PCCP

ROYAL SOCIETY OF CHEMISTRY

PAPER

View Article Online
View Journal | View Issue

Cite this: *Phys. Chem. Chem. Phys.*, 2020, **22**, 21360

A simple molecular design for tunable two-dimensional imine covalent organic frameworks for optoelectronic applications†

Vivek K. Yadav, [a] Showkat H. Mir, [b] Vipin Mishra, [b] Thiruvancheril G. Gopakumar *[b] and Jayant K. Singh *[a]

Received 2nd June 2020,
Accepted 1st September 2020

DOI: 10.1039/d0cp02961k

rsc.li/pccp

Two-dimensional covalent organic frameworks (2D-COFs) belong to a new class of molecular materials that have attracted huge attention in recent years due to their analogous nature to graphene. In this work, we present a systematic study of the electronic structure, carrier mobility and work function of imine based 2D-COFs. We identify these 2D-COFs as a new class of semiconducting materials with tunable electronic/optoelectronic properties and significant mobility. The results show that by rationally doping 2D-COFs at the molecular level, it is possible to control their structural and optoelectronic responses. Cohesive energy calculations revealed that all the studied 2D-COFs are thermodynamically stable. Also, the calculated binding energy of 2D-COFs on HOPG was found to be less than 1 eV, which indicates that the COFs do not interact strongly with HOPG, and it will not affect their electronic properties. Additionally, we have synthesized a 2,4,6-pyrimidinetriamine based 2D-COF and experimentally measured its band gap using scanning tunnelling spectroscopy. The experimentally measured band gap is found to be in good agreement with theoretical results.

1 Introduction

Recent decades have witnessed a surge of exploration of various applications of Covalent Organic Frameworks (COFs), which are composed mainly of lightweight elements such as hydrogen, boron, carbon, nitrogen, and oxygen, primarily linked by a covalent bond network. Since the first 2D-COF was reported by Yagi and coworkers in 2005,[1] research on 2D-COFs has shown significant progress, with a variety of applications like gas storage,[2,3] chemical separation,[4,5] catalysis,[6,7] and sensors,[8,9] as well as optoelectronic[10,11] and energy storage devices.[12,13] Two dimensional COFs (2D-COFs) are formed by covalently linking two organic molecules of interest. 2D-COFs formed by electron rich molecules with aromatic linkages show an undisrupted flow of charge carriers within 2D sheets[14–16] and are thus analogous to other 2D materials, including graphene. Further, the electronic properties are highly tunable in such 2D-COFs and can be controlled by the selection of electron rich molecules. The planar 2D layer consists of a thin layer of single atomic thickness, which can be arranged into a multilayer structure through π–π stacking. The π–π interactions between the stacked layers are considerably weak in these 2D-COF nanosheets. Compared to the bulk COF, single 2D nanosheets of 2D-COF materials with a uniform distribution of electron rich organic chromophores show excellent electron/hole transport properties. Further, a desirable selection of precursor molecules with heteroatoms (O, N) helps to maintain the uniform doping of heteroatoms in the 2D COF, which is typically random in the case of post-doping graphene.[17,18] 2D-COFs can be tuned according to structure-oriented and function-oriented protocols depending on the property of interest. Recently synthesized 2D-COFs have shown very good stability not only in air but also in acid and base media,[19–21] which has led to the exploration of these materials for applications such as photocatalytic water splitting, where aqueous stability is a key requisite. The high crystallinity of a 2D-COF can be retained by a recently developed synthetic methodology which allows consecutive 2D-COF sheets to lock in position during crystal growth and minimizes stacking faults and dislocations.[6,22] Using a series of triphenylarylaldehydes with the central aryl ring containing 0–3 nitrogen atoms as building blocks, Vyas and coworkers synthesized two-dimensional (2D) azine-linked COFs for hydrogen evolution from the photo-catalytic reduction

[a] *Department of Chemical Engineering, Indian Institute of Technology Kanpur, Kanpur, 208016, India. E-mail: gopan@iitk.ac.in*
[b] *Department of Chemistry, Indian Institute of Technology Kanpur, Kanpur, 208016, India. E-mail: jayantks@iitk.ac.in*

† Electronic supplementary information (ESI) available: Optimized structures of 2D-COFs on HOPG, band gap variation, AFM topograph and phase image of 2N-COF prepared from TCA and PTA, STM topographs of 2N-COF, zoomed-in view of the band structure, PDOS, work function, and optimized coordinates. See DOI: 10.1039/d0cp02961k

of water which reflect the structural variations of the triphenylarene moiety.[23] Tuning of the Fermi level of 2D and 3D conjugated polymers has been reported and applied to COF materials in order to tune their properties in ways not available to graphene.[24]

The semi-conductive and photo-conductive properties of COFs were firstly reported by Jiang and coworkers. The synthesized triphenylene-COF (TP-COF) shows semi-conducting character and strong blue light emission, while polypyrene-COF (PPy-COF) is able to harvest visible light and generates a prominent photo-current upon light irradiation.[25,26] Due to the ease of tuning better capabilities by tailoring the organic precursors,[14–16,27,28] the optical and electronic properties of the resulting 2D COFs open an interesting avenue of research with a wide range of potential photo-functional applications.

Herein, we present a study of imine based COFs and show that their band gap can be tailored by nitrogen doping. We performed DFT to show that the band gap of the COFs can be tuned by varying the number of nitrogen atoms. Such COFs can be prepared experimentally using different amines, namely (1) 1,3,5-benzenetriamine (0N), (2) 2,4,6-pyridinetriamine (1N), (3) 2,4,6-pyrimidinetriamine (2N), and (4) 2,4,6-triamino-1,3,5-triazine (3N), in combination with 1,3,5-benzenetricarbaldehyde (TCA) for formation on highly oriented pyrolytic graphite (HOPG) (see Fig. 1). A representative example of the formation of a 2D COF by the reaction between (d) and (e) is shown in Fig. 1(f). Furthermore, we have synthesized 2N-COF on HOPG using 2,4,6-pyrimidinetriamine and 1,3,5-benzenetricarbaldehyde. The 2N-COF is prepared and characterized as per the previously reported established method.[29]

2 Results and discussion

2.1 Theoretical and experimental findings

The progressive substitution of alternate carbon atoms by nitrogen atoms in the central ring of the imine moiety (Fig. 1, blue dots) leads to a change in the electronic and steric properties of the structure, *i.e.*, $N = 0$, $N = 1$, $N = 2$, $N = 3$ (hereafter, these will be called 0N-COF, 1N-COF, 2N-COF, and 3N-COF). In each unit cell, there are 27, 26, 25 and 24 atoms, and the ratio of N atoms increases as 0%, 20%, 60% and 80%, respectively. As a result of the substitution of the C–H moiety with nitrogen atoms, a change in dihedral angle between different imine rings is expected, which in turn leads to varied degrees of planarity in the structure. This was validated by density functional theory calculations. These 2D COFs can be synthesized using melamine and 1,3,5-benzenetricarbaldehyde as precursors, as shown in Fig. 1 (d + e → f). Fig. S1 (ESI†) shows the optimized structures of the imine based 2D COFs studied in the present work on HOPG substrate. The average distance of various COFs from the top layer of HOPG was found to be 3.475 ± 0.002 Å. Also, we observed that the COFs exhibited slight buckling in these structures, varying from 0N to 3N. The vertical upward or downward buckling from the plane was about ± 0.173 Å. The optimized lattice constants of COFs obtained using the PBE(+D2) functional are 10.974 Å, 10.955 Å, 11.092 Å and 11.232 Å for 3N, 2N, 1N and 0N COF, respectively. The maximum pore size calculated for the COFs was 11.20 Å. In order to find out whether these 2D COFs are easily exfoliable from the HOPG, we calculated their binding strength with HOPG using the equation $E_{bind} = E_{COF+HOPG} - E_{COF} - E_{HOPG}$. The binding energy ($E_{bind}$) calculated with BLYP and PBE+D2 functional is displayed in Table 1. The results demonstrated that COFs exhibit physical interaction with HOPG. Hence, these 2D COFs can be peeled off from HOPG without affecting their properties for device application. Furthermore, the thermodynamic stability of the COFs was also assessed by calculating the cohesive energy, employing the equation

$$E_{coh} = \left[E_{COF} - \sum_i n_i E_i\right]/n \quad (i = C, N, H), \qquad (1)$$

where E_{COF} denotes the total energy of the 2D COF, E_i represents the gas phase atomic energies of C, N and H, and n is the total number of atoms in the COF. From this equation, a negative cohesive energy signifies that the system is energetically stable, while a positive value implies instability from an energy point of view. The cohesive energies per atom calculated for the 2D COFs are given in Table 1. From the calculated cohesive energies, we found that the stability of COFs increases

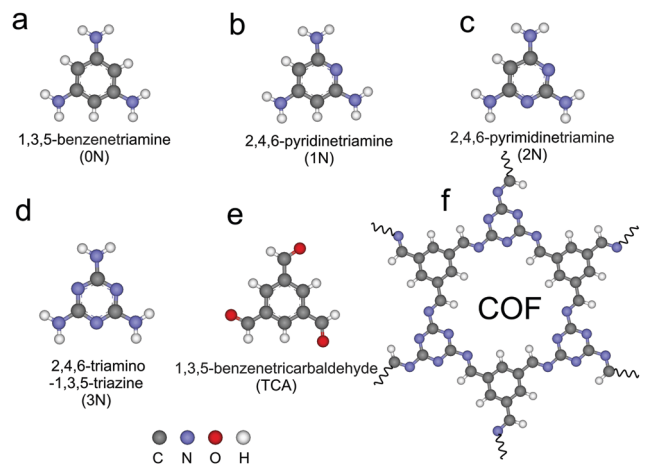

Fig. 1 Structures of (a–d) amines, (e) aldehyde and (f) representative 2D COF synthesized from the combination of amine (d) and aldehyde (e).

Table 1 Cohesive energy per atom (E_{coh}) of 2D COFs, their binding energy (E_{bind}) on HOPG sheet, and distance ($d_{COF-HOPG}$) between the COF and the top layer of HOPG

	E_{coh}		E_{bind}		$d_{COF-HOPG}$	
System	BLYP+D2	PBE+D2	BLYP+D2	PBE+D2	BLYP+D2	PBE+D2
3N-COF	−6.788	−7.277	−0.833	−0.944	3.481	3.472
2N-COF	−6.516	−7.164	−0.833	−0.947	3.483	3.475
1N-COF	−6.429	−7.061	−0.836	−0.949	3.483	3.476
0N-COF	−6.351	−6.967	−0.837	−0.956	3.484	3.476

Energies are given in units of eV, and distances are in Å.

as 0N < 1N < 2N < 3N. Thus, 3N-COF is comparatively more stable than the other COFs.

Now, we discuss the electronic structure of various COFs and the effect of nitrogen doping on their bandgap. Band structure calculations revealed that the electronic bandgap of the COFs is changed by varying the nitrogen percentage. The bandgaps of COFs were calculated using different levels of theory, such as generalized gradient approximation (PBE and BLYP) and hybrid functionals (PBE0 and HSE). The calculated bandgap values for various COFs are presented in Table 2. From Fig. 2a, it is observed that the presence of three nitrogen atoms (3N) in the ring pushes away the valence band maximum (VBM) with respect to the Fermi energy, whereas for zero nitrogen atoms (0N) a large bandgap arises due to shifting of the conduction band minimum (CBM) away from the Fermi level. We conclude that the bandgap first decreases from 3N-COF to 1N-COF, then increases again for 0N-COF, as shown in Fig. 2b. Hybrid calculations also showed a similar trend in the bandgap for these COFs (see Fig. S2, ESI†). The calculated bandgaps are 2.473 (2.419), 2.297 (2.264), 2.344 (2.408) and 2.586 eV (2.817 eV) for 0N-, 1N-, 2N- and 3N-COF obtained by employing PBE+D2 (BLYP+D2), respectively. The calculations showed that the bandgaps of 1N- and 2N-COF are lower compared to that of 0N-COF, whereas 3N-COF has a larger bandgap than 0N-COF. All the 2D COFs were found to show a semiconducting bandgap, as shown in Table 2. The bandgaps calculated using hybrid functionals are also given in Table 2. It is clear from Table 2 that both the hybrid functionals predict larger bandgap values of 2D-COFs than PBE+D2 and BLYP+D2. Thus, it is inferred that the hybrid functional HSE (PBE0) overestimates the bandgaps of 2D-COFs. Our PBE+D2 (BLYP+D2) results predict bandgap values in the range of 2.473 (2.419) eV for 0N-COF and 2.586 (2.817) eV for 3N-COF, which lie in the visible region of the spectrum (1.65 eV for red and 3.40 eV for violet). Thus, it is apparent that all the 2D-COFs are potential materials for optoelectronic applications. Semiconducting 2D COFs formed by electron-rich precursor molecules have been also reported previously.[29–31]

Table 2 Theoretically calculated bandgaps of various 2D COFs using different functionals (with D2 correction). All results are given in eV units

	Functional	VBM	CBM	E_{gap}
3N-COF	PBE	−6.226	−3.640	2.586
	BLYP	−6.057	−3.240	2.817
	HSE	−6.996	−3.244	3.752
	PBE0	−7.391	−2.872	4.518
2N-COF	PBE	−5.874	−3.531	2.344
	BLYP	−5.561	−3.152	2.408
	HSE	−6.404	−3.157	3.247
	PBE0	−6.798	−2.785	4.013
1N-COF	PBE	−5.605	−3.308	2.297
	BLYP	−5.127	−2.952	2.264
	HSE	−6.016	−2.941	3.075
	PBE0	−6.410	−2.569	3.840
0N-COF	PBE	−5.453	−2.980	2.473
	BLYP	−5.061	−2.641	2.419
	HSE	−5.867	−2.599	3.267
	PBE0	−7.291	−2.873	4.518

Using an established method,[29] we synthesized 2N-COF on HOPG from 1,3,5-benzenetricarbaldehyde (TCA) and 2,4,6-pyrimidinetriamine (PTA). Further differential conductivity (dI/dV) as a function of sample voltage was performed using scanning tunnelling microscopy. dI/dV is directly related to the local density of states (LDOS). The experimentally measured bandgap value for 2N-COF is ≈2.1 eV, which corresponds to the above mentioned value obtained using DFT calculations (PBE+D2 and BLYP+D2 functionals). Fig. 3a shows the normalized average dI/dV measured on 2N-COF; the black and grey curves represent two independent sets (averaged over 30 measurements) of dI/dV measurements of 2N-COF. The green dashed lines indicate the positions of the valence band maximum (VBM) and conduction band minimum (CBM) and are -1.2 ± 0.1 eV and 0.9 ± 0.1 eV, respectively. The asymmetry in the band gap also correlates well with the theoretically obtained VBM and CBM (see Fig. 2). Since the LDOS of graphite makes a major contribution to the dI/dV measured on 2N-COF on graphite, we extract the LDOS of 2N-COF using a normalization method as follows. The dI/dV of graphite (measured independently for freshly cleaved HOPG) is subtracted from that of 2N-COF on HOPG using the following equation:

$$\frac{dI}{dV}_{\text{2N-COF}} = \frac{dI}{dV}_{\text{2N-COFonHOPG}} - \frac{dI}{dV}_{\text{HOPG}} \times a,$$

where a is a free parameter used for subtracting the dI/dV obtained for graphite alone from that of 2N-COF on graphite.[29] This parameter should represent the extent of the contribution of the graphite LDOS to the dI/dV of 2N-COF on graphite. In the current case we use a = 0.2 after optimizing through trials. Below this value the dI/dV shows a negative contribution. For higher values of a we are unable to observe the gap. The raw dI/dV obtained on 2N-COF on HOPG, along with the normalized dI/dV, is provided in Fig. S3 (ESI†). Fig. 3b shows a STM topograph of 2N-COF on HOPG. Similar frames are used for the dI/dV measurements. The line-like features marked with red dashed lines represent adjacent molecular rows of the COF. The inter-line spacing is ∼6.2 Å, which corresponds to half of the unit cell parameter of the 2N-COF obtained from calculations. This indicates that the adjacent lines correspond to adjacent molecular rows in the 2N-COF. The origin of these lines contrasts with the optimized geometry of 2N-COF (see the lower part of Fig. 3b). The unit cell of the optimized 2N-COF is represented by a black outline and the red dashed lines on the model depict the adjacent molecular rows. The spacing between the red lines in the optimized 2N-COF clearly corresponds to the line-like contrast in the experiment. A 2D COF hexagonal network with a larger pore size was imaged at a solid–air interface.[29] The expected hexagonal pattern could not be observed by STM, which is most likely since the imaging was performed at a solid–air interface and due to the small pore size. The uninterrupted line-like contrast in the STM topograph indicates that the growth of the 2N-COF in single domains is uniform. We observed typical domains of size ∼200 nm. Two types of 2N-COF domain are typically visible, uniform smooth domains (as shown in Fig. 3b) and fractal-like growth with

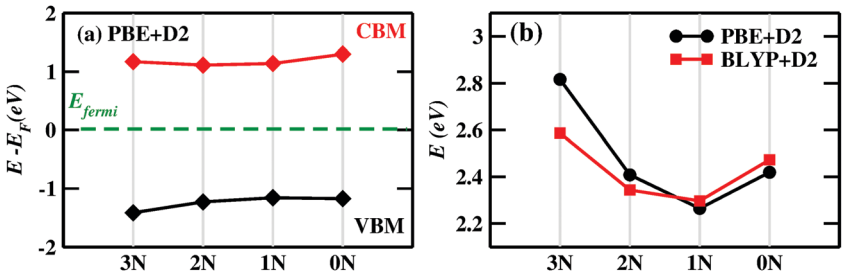

Fig. 2 (a) Plot of the valence band maximum (VBM) and conduction band minimum (CBM) using the PBE+D2 functional for 3N to 0N COFs with respect to their Fermi energy (E_{Fermi}). (b) Variation in bandgap of 2D COFs from 3N to 0N calculated using PBE+D2 and BLYP+D2.

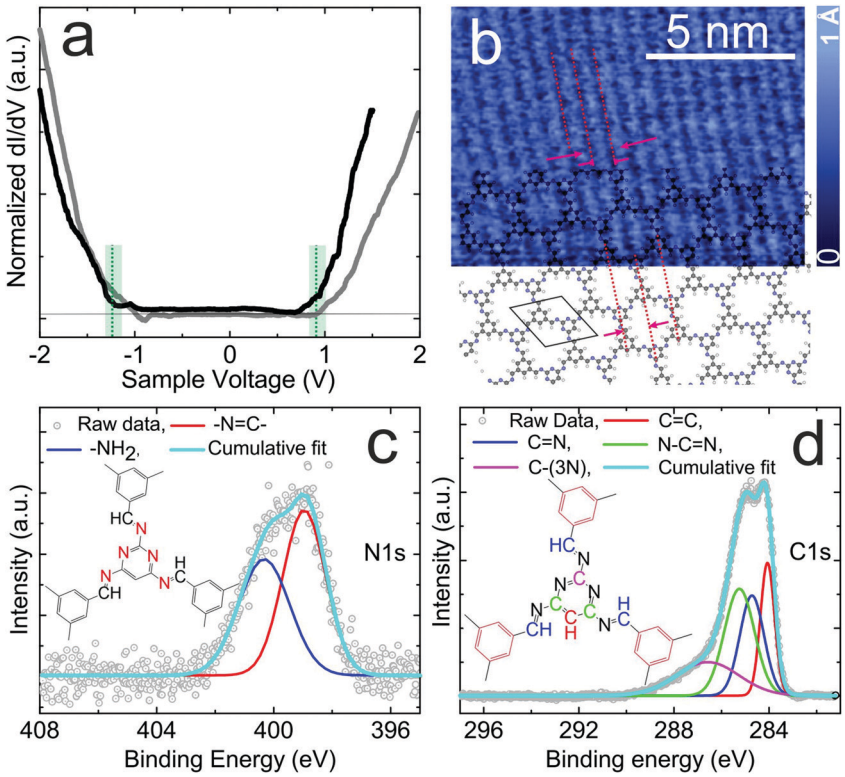

Fig. 3 (a) Normalized differential conductivity (d*I*/d*V*) obtained on 2D 2N-COF at HOPG–air interface. Black and gray curves represent two independent sets of averaged measurements. (b) Constant current STM topograph of 2D 2N-COF on HOPG. Line-like contrast corresponding to adjacent molecular rows in 2N-COF is marked by red dashed lines. The corresponding molecular rows in the DFT optimized geometry (red dashed lines) of 2N-COF are included at the bottom. Outline shows the unit cell of 2N-COF. N1s (c) and C1s (d) resonances observed in the XPS spectra of 2N-COF on HOPG.

interconnected small domains. Additional AFM and STM images of the different types of 2N-COF domain are provided in Fig. S4 and S5 (ESI†), respectively.

To show the formation of 2N-COF we performed X-ray photon electron spectroscopy (XPS) on 2N-COF formed on HOPG (similar sample as used above). Fig. 3c shows the N1s resonance of 2N-COF. Two major resonances are revealed: one at 398.7 eV, corresponding to imine nitrogen (–C═N– bond), and the other at 400.15 eV, corresponding to amine ($-NH_2$). The presence of imine nitrogen in XPS shows the formation of the aromatic linkage in 2N-COF.[29,32] The amine nitrogen is expected from the unreacted regions of 2N-COF on the surface. As revealed in AFM and STM, there are fractal-like domains which possess large edges, and therefore amine nitrogen is reasonable. The XPS N1s resonance obtained on 2,4,6-pyrimidinetriamine film (precursor of 2N-COF) shows a major resonance that corresponds to free amine at 400.07 eV (see data in S5, ESI†). Upon formation of 2N-COF the free amine concentration decreases rapidly. In addition, the formation of 2N-COF is also confirmed from the C1s resonance observed in the XPS data obtained from 2N-COF. Resonances corresponding to –C═N–, –N–C═N– and $-C(N)_3$ type carbon are expected compared to pure carbon on bare graphite surface. Different types of C1s resonances are shown in Fig. 3d: sp^2 –C═C– (284.1 eV), sp^2 –C═N– (284.7 eV), sp^2 –N–C═N– (285.25 eV), and sp^2 C bonded to three N ($-C(N)_3$, 286.6 eV). XPS spectra of

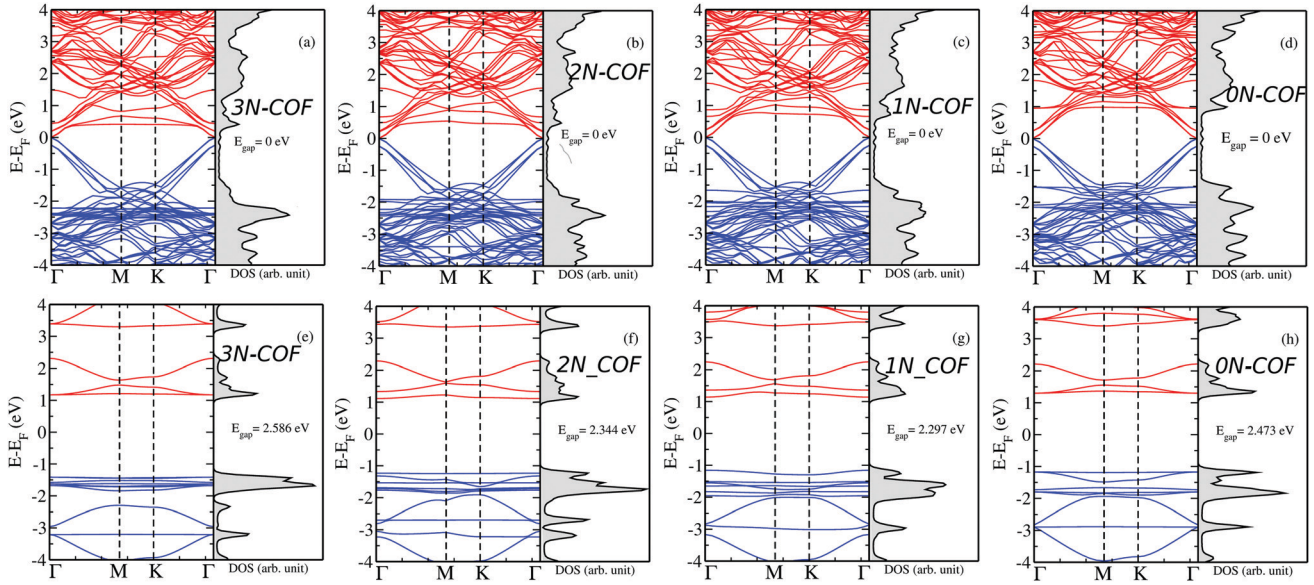

Fig. 4 Calculated band structures of (a–d) 2D COFs on HOPG and (e–h) in free-standing configuration using PBE+D2 functional.

2,4,6-pyrimidinetriamine film and freshly cleaved HOPG are shown in Fig. S6 (ESI†).

The calculated band structures of 2D COFs in pristine form and on HOPG are shown in Fig. 4. It can be seen that the band structure (Fig. 4(a–d)) is essentially a superposition of the two independent band structures of HOPG and the 2D COF. We also observe that all 2D COFs exhibit a direct bandgap at the Γ-point of the Brillouin zone (Fig. 4(e–h)).

Further, for 0N- and 3N-COFs, it can be seen that the bands forming conduction band edges exhibit degeneracy along the Γ–M direction of the Brillouin zone, while there is no degeneracy of the bands in 1N- and 2N-COFs. This behavior in the conduction band edge can be explained on the basis of symmetry of the central imine ring. The central ring is symmetric in 0N- and 3N-COFs but asymmetric in 1N- and 2N-COFs, which is the reason for obtaining degenerate bands along the Γ–M direction in 0N- and 3N-COFs. It is also interesting to see that as we go from 3N- to 0N-COF, the valence band edge shifts upwards towards the Fermi level. To clearly visualize this effect, we also plotted a zoomed-in view of the band structure of pristine COFs in Fig. S7 (ESI†). From Fig. S7 (ESI†), it can be clearly seen that the valence band edge of 2N- and 1N-COFs is shifted upwards by ∼0.2 and ∼0.3 eV, respectively, and the conduction band edge is moved slightly downwards with respect to 3N-COF. On the other hand, the valence band edge of 0N-COF is shifted upwards, but at the same time, its conduction band edge also shifts upwards. This clearly demonstrates why the bandgap first decreases for 2N- and 1N-COF and then increases for 0N-COF, as depicted in Fig. 2.

To explore the nature of the conduction and valence band edges and the charge transfer in aromatic linkages, we calculated the partial density of states (PDOS) of 2D COFs using PBE+D2, as shown in Fig. 5 (for PDOS calculated using BLYP+D2 functional see Fig. S8, ESI†). From the calculated PDOS, it is clear that most of the conducting states in the COFs originate mainly from carbon p orbitals. The valence band edges of 3N- and 2N-COFs are dominated by nitrogen p orbitals. On the other hand, for 1N- and 0N-COFs the valence band edges mainly arise from carbon p orbitals. Thus, it is presumed that charge transfer may take place from carbon to carbon in 0N- and 1N-COFs, and nitrogen to carbon in 2N- and 3N-COFs. To further explore the distribution of charges, we plotted the highest occupied molecular orbital (VBM) and lowest unoccupied molecular orbital (CBM) at the Fermi level in various COFs for the Γ-point (Fig. 6). It can be seen that in the VBM, charge distribution in 3N- and 2N-COFs is distributed

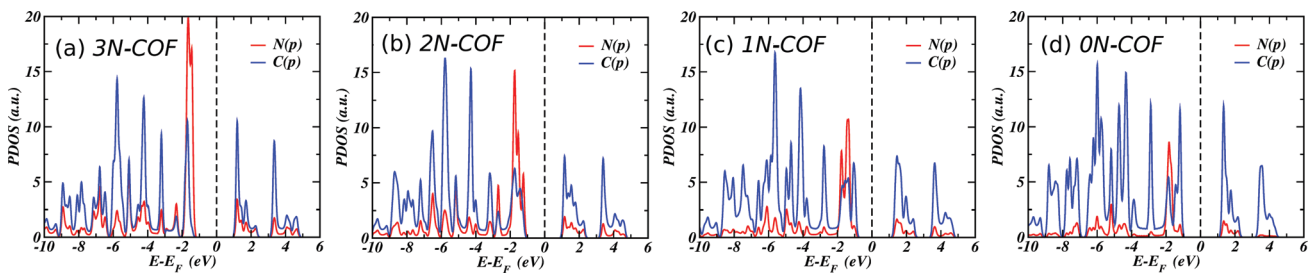

Fig. 5 Partial density of states (PDOS) of 2D COFs from 3N to 0N calculated using PBE+D2 functional.

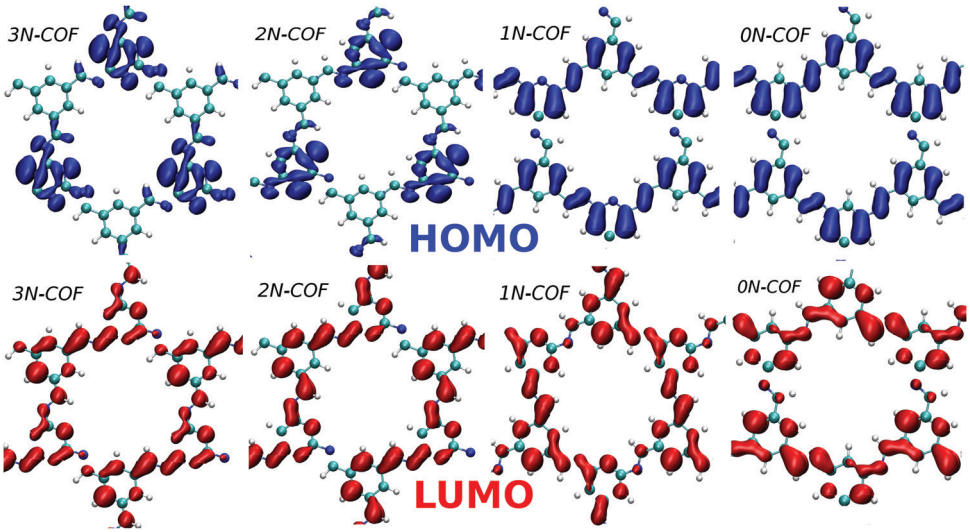

Fig. 6 VBM/CBM plots of 2D COFs from 3N to 0N calculated using PBE+D2 functional. The isosurface value is set to 0.00138 e Å^{-3}. Blue and red lobes represent the VBM and CBM, respectively.

over the nitrogen atoms, while in 1N- and 0N-COFs, it is dispersed over C atoms with a small contribution from N atoms, as can be seen from PDOS (Fig. 5(c and d)). On the other hand, one can see from Fig. 6 that the CBM is distributed throughout the framework, originating mainly from carbon atoms. Nevertheless, it is worth mentioning that in the triazine/nitrogen doped moiety, each nitrogen atom is bonded to only two carbons, leaving an unpaired electron and a lone pair in the system. This accounts for the catalytic active sites of g-C_3N_4, as reported by Wang *et al.*[33] This leads to different bandgaps in the COFs presented here. In short, varying the percentage of N atoms in COFs is crucial for electronic properties and plays a critical role in tuning their band gap and thus optoelectronic activity.

The work function (Φ) of 2D COFs was also calculated using the PBE+D2 functional. The work function is defined as the energy required to remove an electron from the Fermi level to the vacuum and was calculated using eqn (2):

$$\Phi = E_{\text{vac}} - E_{\text{F}}, \tag{2}$$

where E_{vac} represents the vacuum potential and E_{F} is the Fermi energy. Thus, the work function is determined by calculating the average electrostatic vacuum potential of a 2D-COF and then subtracting from it the Fermi energy. We found that the work function increases as the nitrogen percentage in the COF is increased. Thus, it is found that the work function is maximum for 3N-COF and minimum for 0N-COF. The values of Φ calculated were 5.209, 5.033, 4.855 and 4.711 eV from 3N to 0N-COFs, respectively. Plots of the work function are shown in Fig. S9 (ESI†). These results clearly show that the work function of COFs can also be tuned *via* nitrogen doping.

2.2 Carrier transport

The electron/hole mobility in a semiconductor is mainly limited due to scattering by phonons or defects. The former are also responsible for the temperature dependence of electrical conductivity. In this work, we calculated the mobility of different COFs using deformation potential theory and the effective mass approximation. In this approximation, the phonon-limited mobility of charge carriers in a 2D semiconductor along a given direction is calculated using the following equation:[34,35]

$$\mu = \frac{e\hbar^3}{\lambda m^{*2}}, \tag{3}$$

where m^* is the carrier effective mass and λ is the scattering probability for the charge carriers along the transport direction. The scattering probability is calculated as

$$\lambda = \frac{k_B T (E_i)^2}{C_{2D}}. \tag{4}$$

Here, C_{2D} is the elastic constant, T is the temperature (300 K) and E_i is the deformation potential, which is defined as

$$E_i = \Delta E_i/\varepsilon \quad i = \text{CBM/VBM}, \tag{5}$$

where $\varepsilon(=\Delta a/a)$ is the applied strain. ΔE_i is the change in energy of the i^{th} band with respect to vacuum potential. The deformation potential is obtained by a linear fit of ΔE_i *versus* strain, where the strain is varied from −2% to 2%. The elastic modulus measures the in-plane stiffness and is calculated using the equation $(E - E_0)/A_0 = \frac{1}{2}C_x\varepsilon^2$, where A_0 and E_0 represent the equilibrium area and energy of the system and E is the energy of the strained system. The effective mass is defined as $m^{*-1} = \frac{1}{\hbar^2}\frac{\partial^2 E}{\partial k^2}$ and is determined by parabolic fitting of the E *versus* k curve for holes and electrons in the vicinity of the VBM and CBM, respectively. The calculated mobility and the corresponding values of C and λ are listed in Table 3. From the table, it is apparent that the carrier mobility follows the same trend as the band gap of various COFs. The calculated mobility of

Table 3 Calculated elastic constants (C), effective mass (m^*/m), scattering probability (λ) and mobility (μ) of various 2D COFs at 300 K. Here, e = electron, h = hole, and m = mass of electron

	Carrier type	C (J m^{-2})	(m^*/m)	λ (eV^2 Å^2)	μ (10^3 cm^2 V^{-1} s^{-1})
3N	e	49.754	0.402	0.276	0.198
	h	49.754	0.513	0.236	0.142
2N	e	47.967	0.474	0.006	6.562
	h	47.967	0.761	0.186	0.082
1N	e	50.018	0.153	0.047	8.082
	h	50.018	0.135	0.466	1.034
0N	e	46.630	0.278	0.315	0.364
	h	46.630	0.928	0.233	0.044

different COFs covers a range from 10^2 to 10^3, which is significantly larger than expected for 2D-COFs. Thus, it is evident that DP theory highly overestimates the mobilities of 2D-COFs; hence, it should be applied to such COFs judiciously.[36]

We also extracted the conductivity of all COFs as a function of temperature using the Boltztrap code.[37] The conductivity (σ/τ) as a function of temperature is shown in Fig. 7. We found that both Boltztrap and deformation potential theory predict the same trend for the carrier transport properties of various COFs. Nevertheless, it is apparent from the figure that conductivity exists at high temperatures, as expected.

3 Methods

3.1 Computational details

Ab initio calculations were performed within the framework of DFT using a plane wave ultrasoft pseudopotential[38] method as implemented in the Quantum ESPRESSO package.[39,40] The exchange correlation between electrons was described by GGA approximation using Perdew–Burke–Ernzerhof[41] (PBE) and BLYP[42,43] functionals. Apart from the BLYP and PBE functionals, we employed the hybrid functionals PBE0[44] and HSE[45] that yield accurate bandgap values. The electron wavefunctions were expanded in a plane wave basis set using kinetic energy cutoffs of 40 Ry and 320 Ry for charge density. A set of calculations was performed to evaluate the best kinetic energy cutoff and k-point grid (Fig. S10, ESI†). Brillouin zone integrations were carried out with a uniform k-mesh of 5 × 5 × 1 for relaxation and 10 × 10 × 1 for scf calculation. The relaxation calculations were done until the magnitude of the Hellmann–Feynman force on each ion was less than 0.03 eV A^{-1}. vdW interactions were also included in the calculations using Grimme's D2 corrections.[46]

The carrier mobilities were calculated using the semi-classical Boltzmann equation under a constant relaxation approximation as implemented in the Boltztrap code.[37] A dense k-mesh of 40 × 40 × 1 was used for transport property calculations. Indeed, the constant relaxation time approximation has been widely used in theoretical calculations of thermoelectric materials and has successfully predicted the temperature and carrier concentration dependence of the transport properties for some materials with non-parabolic band structures.[47] Deformation potential theory[35,48] was also used to calculate the electron and hole mobility separately and the results were compared with Boltzmann theory.

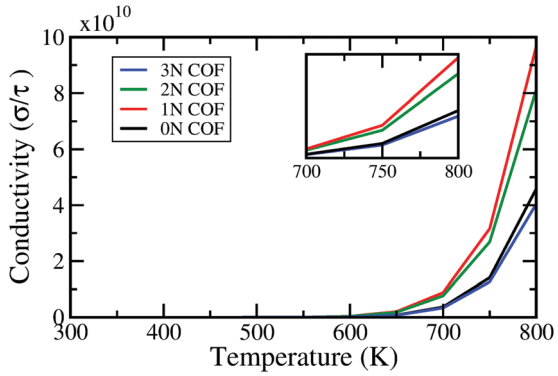

Fig. 7 Conductivity (Ω^{-1} cm^{-1} s^{-1}) as a function of temperature. The inset shows a zoomed-in view of the conductivity between 700 and 800 K.

3.2 Experimental details

TCA (1,3,5-benzenetricarbaldehyde; purity 99%) and PTA (2,4,6-pyrimidinetriamine; purity 99%) purchased from Sigma Aldrich are used for the experiments with no further purification. The solutions are prepared in diglyme (HPLC grade, 99.9%; from Avra). TCA and PTA molecules are dissolved in a mixture of diglyme and methanol and sonicated for 30 minutes. Equimolar concentrations (10^{-2} M) of TCA and PTA are mixed in a 1 : 1 ratio (1 μm glacial acetic acid is added) and heated to a temperature of 150 °C for ~1 h (until the solution turns yellowish). The stock solution (~10^{-2} M) is diluted to a concentration of 10^{-4} M in methanol (HPLC grade, 99:9; from Merck) and drop-casted (~2 μl) on a freshly cleaved HOPG surface. The drop-casted HOPG is transferred to a reaction chamber which has a continuous supply of N_2 gas moistened with water.[49] The reaction chamber is heated to a temperature of ~300 °C for 5 hours. This sample is used for the STM and AFM measurements under ambient conditions. RHK STM and Agilent-5500 AFM are used for sample analysis. Mechanically cut Pt/Ir wires are used as STM tips. We use intermittent contact mode AFM (also referred to as AC Mode due to the alternating contact of the tip with the surface). AFM images are obtained using PPP-NCH silicon cantilevers purchased from Nanosensors (300 kHz, 35 N m^{-1}), which are designed for intermittent contact mode of operation. A feedback system is employed to maintain the oscillation amplitude at a set point value. The difference between the amplitude and the set point, called the "error signal", is used as the input of the feedback system. A constant average force is maintained during the measurement. All the AFM and STM images are post-processed and analyzed using WSxM.

4 Conclusions

Using first principles calculations, we have systematically investigated the electronic structure and work function of a series of free-standing 2D imine based COFs. We found that the

bandgap of the COFs can be tailored by doping with nitrogen. Our findings show that the bandgaps of 0N and 1N COFs lie in the visible spectrum, which makes them suitable for optoelectronic applications. Also, we found that although the bandgaps of the other two COFs are slightly larger than those of the previously mentioned COFs, nevertheless their bandgaps still lie in the UV-visible range. These findings show that imine based COFs may be a new family of materials for optoelectronic applications. Our theoretical results are expected to stimulate experimentalists to further study novel 2D metal-free organic materials as UV-visible light optoelectronic materials with unique advantages. More importantly, our strategies for designing and modifying 2D organic materials may further encourage scientists to search for other unknown 2D organic materials in the future, which will broaden the scope and scientific impact of organic materials and devices. It is also observed that the carrier mobilities of the COFs are consistent with the calculated band gaps.

Conflicts of interest

There are no conflicts to declare.

Acknowledgements

VKY acknowledges the funding from Department of Science and Technology (MHRD F. NO. 5-6/2013 TS-VII). SHM gratefully acknowledges the Institute Postdoctoral fellowship (IPDF) from the Department of Chemistry at IIT Kanpur. The authors are thankful to the HPC centre IIT Kanpur for providing computational facilities. VM would like to thank the Council of Scientific and Industrial Research (CSIR) for the research fellowship.

References

1 P. C. Adrien, I. B. Annabelle, W. O. Nathan, O. K. Michael, J. M. Adam and M. Y. Omar, Porous, Crystalline, Covalent Organic Frameworks, *Science*, 2005, **310**, 1166–1170.
2 S. Han, H. Hurukawa, O. M. Yaghi and W. A. Goddard, Covalent Organic Frameworks as Exceptional Hydrogen Storage Materials, *J. Am. Chem. Soc.*, 2008, **130**, 11580–11581.
3 J. L. Mendoza-Cortes, S. S. Han, H. Furukawa, O. M. Yaghi and W. A. Goddard, Adsorption Mechanism and Uptake of Methane in Covalent Organic Frameworks: Theory and Experiment, *J. Phys. Chem. A*, 2010, **114**, 10824–10833.
4 C. Yang, C. Liu, Y. Caoa and X. Yan, Facile Room-Temperature Solution-Phase Synthesis of a Spherical Covalent Organic Framework for High-Resolution Chromatographic Separation, *Chem. Commun.*, 2015, **51**, 12254–12257.
5 S. J. Keskin, Adsorption, Diffusion, and Separation of CH_4/H_2 Mixtures in Covalent Organic Frameworks: Molecular Simulations and Theoretical Predictions, *J. Phys. Chem. C*, 2012, **116**, 1772–1779.
6 H. Xu, J. Gao and D. Jiang, Stable, Crystalline, Porous, Covalent Organic Frameworks as a Platform for Chiral Organocatalysts, *Nat. Chem.*, 2015, **7**, 905–912.
7 S. Lin, C. S. Diercks, Y. Zhang, N. Kornienko, E. M. Nichols, Y. Zhao, A. R. Paris, D. Kim, P. Yang, O. M. Yaghi and C. J. Chang, Covalent Organic Frameworks Comprising Cobalt Porphyrins for Catalytic CO_2 Reduction in Water, *Science*, 2015, **349**, 1208–1213.
8 G. Das, B. P. Biswal, S. Kandambeth, V. Venkatesh, G. Kaur, M. Addicoat, T. Heine, S. Verma and R. Banerjee, Chemical Sensing in Two Dimensional Porous Covalent Organic Nanosheets, *Chem. Sci.*, 2015, **6**, 3931–3939.
9 S. Dalapati, S. Jin, J. Gao, Y. Xu, A. Nagai and D. Jiang, An Azine-Linked Covalent Organic Framework, *J. Am. Chem. Soc.*, 2013, **135**, 17310–17313.
10 J. Guo, Y. Xu, S. Jin, L. Chen, T. Kaji, Y. Honsho, M. A. Addicoat, J. Kim, A. Saeki, H. Ihee, S. Seki, S. Irle, M. Hiramoto, J. Gao and D. Jiang, Conjugated Organic Framework with Three-Dimensionally Ordered Stable Structure and Delocalized π Clouds, *Nat. Commun.*, 2013, **4**, 2736.
11 M. Dogru, M. Handloser, F. Auras, T. Kunz, D. Medina, A. Hartschuh, P. Knochel and T. Bein, A Photoconductive Thienothiophene-Based Covalent Organic Framework Showing Charge Transfer Towards Included Fullerene, *Angew. Chem., Int. Ed.*, 2013, **52**, 2920–2924.
12 C. R. DeBlase, K. E. Silberstein, T. Truong, H. D. Abrun and W. R. Dichtel, β-Ketoenamine-Linked Covalent Organic Frameworks Capable of Pseudocapacitive Energy Storage, *J. Am. Chem. Soc.*, 2013, **135**, 16821–16824.
13 C. R. DeBlase, K. Hernandez-Burgos, K. E. Silberstein, G. G. Rodraguez Calero, R. P. Bisbey, A. H. D. Abrun and W. R. Dichtel, Rapid and Efficient Redox Processes Within 2D Covalent Organic Framework Thin Films, *ACS Nano*, 2015, **9**, 3178–3183.
14 R. Gutzler and D. F. Perepichka, π-Electron Conjugation in Two Dimensions, *J. Am. Chem. Soc.*, 2013, **135**, 16585–16594.
15 P. Zhu and V. Meunier, Electronic Properties of Two-Dimensional Covalent Organic Frameworks, *J. Chem. Phys.*, 2012, **137**, 244703.
16 Y. Zhou, Z. Wang, P. Yang, X. Zu and F. Gao, Electronic and Optical Properties of Two-Dimensional Covalent Organic Frameworks, *J. Mater. Chem.*, 2012, **22**, 16964–16970.
17 S. Feng, M. C. Santos, B. R. Carvalho, R. Lv, Q. Li, K. Fujisawa, A. L. Elias, Y. Lei, N. Perea-Lopez and M. Endo, *et al.*, Ultrasensitive Molecular Sensor Using N-Doped Graphene Through Enhanced Raman Scattering, *Sci. Adv.*, 2016, **2**, e1600322.
18 X. Wang, X. Li, L. Zhang, Y. Yoon, P. K. Weber, H. Wang, J. Guo and H. Dai, N-Doping of Graphene Through Electrothermal Reactions with Ammonia, *Science*, 2009, **324**, 768–771.
19 S. Dalapati, S. Jin, J. Gao, Y. Xu, A. Nagai and D. Jiang, An azine-Linked Covalent Organic Framework, *J. Am. Chem. Soc.*, 2013, **135**, 17310–17313.
20 S. Kandambeth, A. Mallick, B. Lukose, M. V. Mane, T. Heine and R. Banerjee, Construction of Crystalline 2D Covalent Organic Frameworks with Remarkable Chemical (Acid/Base) Stability via a Combined Reversible and Irreversible Route, *J. Am. Chem. Soc.*, 2012, **134**, 19524–19527.

21 B. P. Biswal, S. Chandra, S. Kandambeth, B. Lukose, T. Heine and R. Banerjee, Mechanochemical Synthesis of Chemically Stable Isoreticular Covalent Organic Frameworks, *J. Am. Chem. Soc.*, 2013, **135**, 5328–5331.

22 L. Ascherl, T. Sick, J. T. Margraf, S. H. Lapidus, M. Calik, C. Hettstedt, K. Karaghiosoff, M. Doblinger, T. Clark, K. W. Chapman, F. Auras and T. Bein, Molecular Docking Sites Designed for the Generation of Highly Crystalline Covalent Organic Frameworks, *Nat. Chem.*, 2016, **8**, 310–316.

23 V. S. Vyas, F. Haase, L. Stegbauer, G. Savasci, F. Podjaski, C. Ochsenfeld and B. V. Lotsch, A Tunable Azine Covalent Organic Framework Platform for Visible Light-Induced Hydrogen Generation, *Nat. Commun.*, 2015, **6**, 8508.

24 J. J. Adjizian, P. Briddon, B. Humbert, J. L. Duvail, P. Wagner, C. Adda and C. Ewels, Dirac Cones in Two-Dimensional Conjugated Polymer Networks, *Nat. Commun.*, 2014, **5**, 5842.

25 S. Wan, J. Guo, J. Kim, H. Ihee and D. L. Jiang, A Belt-Shaped, Blue Luminescent, and Semiconducting Covalent Organic Framework, *Angew. Chem., Int. Ed.*, 2008, **47**, 8826–8830.

26 S. Wan, J. Guo, J. Kim, H. Ihee and D. L. Jiang, A Photoconductive Covalent Organic Framework: Self-Condensed Arene Cubes Composed of Eclipsed 2D Polypyrene Sheets for Photocurrent Generation, *Angew. Chem., Int. Ed.*, 2009, **48**, 5439–5442.

27 B. Lukose, A. Kuc and T. Heine, Stability and Electronic Properties of 3D Covalent Organic Frameworks, *J. Mol. Model.*, 2013, **19**, 2143–2148.

28 R. S. Sprick, *et al.*, Tunable Organic Photocatalysts for Visible-light-driven Hydrogen Evolution, *J. Am. Chem. Soc.*, 2015, **137**, 3265–3270.

29 V. Mishra, V. K. Yadav, J. K. Singh and T. G. Gopakumar, Electronic Structure of a Semi-Conducting Imine-Covalent Organic Framework, *Chem. – Asian J.*, 2019, **14**, 4645–4650.

30 E. Jin, M. Asada, Q. Xu, S. Dalapati, A. M. Addicoat, M. A. Brady, H. Xu, T. Nakamura, T. Heine, Q. Chen and D. Jiang, Two-dimensional sp^2 Carbon-conjugated Covalent Organic Frameworks, *Science*, 2017, **357**, 673–676.

31 S. Wan, F. Gándara, A. Asano, H. Furukawa, A. Saeki, S. K. Dey, L. Liao, M. W. Ambrogio, Y. Y. Botros, X. Duan, S. Seki, J. F. Stoddart and O. M. Yaghi, Covalent Organic Frameworks with High Charge Carrier Mobility, *Chem. Mater.*, 2011, **23**, 4094–4097.

32 H. A. Ma, X. P. Jia, L. X. Chen, P. W. Zhu, W. L. Guo, X. B. Guo, Y. D. Wang, S. Q. Li, G. T. Zou, G. Zhang and P. Bex, *J. Phys.: Condens. Matter*, 2002, **14**, 11269–11273.

33 W. Yong, X. Wang and M. Antonietti, Polymeric Graphitic Carbon Nitride as a Heterogeneous Organocatalyst: from Photochemistry to Multipurpose Catalysis to Sustainable Chemistry, *Angew. Chem., Int. Ed.*, 2012, **51**, 68–89.

34 J. Xi, M. Long, L. Tang, D. Wang and Z. Shuai, First-principles Prediction of Charge Mobility in Carbon and Organic Nanomaterials, *Nanoscale*, 2012, **4**, 4348–4369.

35 V. K. Yadav, S. H. Mir and J. K. Singh, A computational study of structural, electronic and carrier mobility of boron and phosphorus/nitrogen co-doped graphene, *Phys. B*, 2019, **571**, 291–295.

36 J. Yu and T. Heine, Two-dimensional Kagome Lattices Made of Hetero Triangulenes are Dirac Semimetals or Single-Band Semiconductors, *J. Am. Chem. Soc.*, 2018, **141**, 743–747.

37 G. Madsen and D. B. Singh, A Code for Calculating Band-structure Dependent Quantities, *Comput. Phys. Commun.*, 2006, **175**, 67–71.

38 D. Vanderbilt, Soft Self-Consistent Pseudopotentials in a Generalized Eigenvalue Formalism, *Phys. Rev. B: Condens. Matter*, 1990, **41**, 7892–7895.

39 P. Giannozzi, O. Andreussi, T. Brumme, O. Bunau, M. B. Nardelli, M. Calandra, R. Car, C. Cavazzoni, D. Ceresoli and M. Cococcion, *et al.*, QUANTUM ESPRESSO: a Modular and Open-source Software Project for Quantum Simulation of Materials, *J. Phys.: Condens. Matter*, 2009, **21**, 395502.

40 P. Giannozzi, O. Andreussi, T. Brumme, O. Bunau, M. B. Nardelli, M. Calandra, R. Car, C. Cavazzoni, D. Ceresoli and M. Cococcion, *et al.*, Advanced Capabilities for Materials Modelling with Quantum ESPRESSO, *J. Phys.: Condens. Matter*, 2017, **29**, 465901.

41 J. P. Perdew, K. Burke and M. Ernzerhof, Generalized Gradient Approximation made Simple, *Phys. Rev. Lett.*, 1996, **77**, 3865–3868.

42 A. D. Becke, Density-Functional Exchange-Energy Approximation with Correct Asymptotic Behavior, *Phys. Rev. A: At., Mol., Opt. Phys.*, 1988, **38**, 3098–3100.

43 C. Lee, W. Yang and R. G. Parr, Development of the Colle-Salvetti Correlation-Energy Formula into a Functional of the Electron Density, *Phys. Rev. B: Condens. Matter Mater. Phys.*, 1988, **37**, 785–789.

44 C. Adamo and V. Barone, Toward Reliable Density Functional Methods Without Adjustable Parameters: The PBE0 Model, *J. Chem. Phys.*, 1999, **110**, 6158–6170.

45 J. Heyd, G. E. Scuseria and M. Ernzerhof, Hybrid Functionals Based on a Screened Coulomb Potential, *J. Chem. Phys.*, 2003, **118**, 8207–8215.

46 S. Grimme, Semiempirical GGA-type Density Functional Constructed with a Long-Range Dispersion Correction, *J. Comput. Chem.*, 2006, **27**, 1787–1799.

47 D. Zou, S. Xie, Y. Liu, J. Lin and J. Li, Electronic Structures and Thermoelectric Properties of Layered BiCuOCh Oxychalcogenides (Ch= S, Se and Te): First-Principles Calculations, *J. Mater. Chem. A*, 2013, **1**, 8888–8896.

48 J. Xi, M. Long, L. Tang, D. Wang and Z. Shuai, First-principles Prediction of Charge Mobility in Carbon and Organic Nanomaterials, *Nanoscale*, 2012, **4**, 4348–4369.

49 J. F. Dienstmaier, A. M. Gigler, A. J. Goetz, P. Knochel, T. Bein, A. Lyapin, S. Reichlmaier, W. M. Heckl and M. Lackinger, Synthesis of Well-Ordered COF Monolayers: Surface Growth of Nanocrystalline Precursors versus Direct On-Surface Polycondensation, *ACS Nano*, 2011, **5**, 9737–9745.

